Impact of A-site cation substitution on the properties of spinel AY_2O_4 (A = Cd, Zn): A first-principles investigation

K. Hocine[a,b,*], Y. Guermit[a,b], and A. Chaabane[b]

[a] *Thin-film physics and advanced technologies laboratory, University of Relizane, Algeria.*
e-mail: Kamel.hocine@univ-relizane.dz
[b] *University of Relizane, Algeria.*

Received 18 September 2024; accepted 22 May 2025

This study presents a comprehensive first-principles investigation of the structural, electronic, magnetic, elastic, thermodynamic, and optical properties of spinel-type compounds CdY_2O_4 and ZnY_2O_4 using density functional theory (DFT) within the full-potential linearized augmented plane wave (FP-LAPW) method. Structural optimization, performed through Murnaghan equation of state fitting and internal atomic relaxation, reveals that both compounds favor a nonmagnetic normal spinel configuration as their ground state. Electronic band structure calculations using PBE-GGA and TB-mBJ functionals demonstrate that both ZnY_2O_4 and CdY_2O_4 are direct band gap semiconductors, with wide band gaps ranging from 4.86 to 4.93 eV. Elastic constants confirm mechanical stability, with CdY_2O_4 exhibiting ductile behavior and ZnY_2O_4 displaying higher stiffness but slightly brittle characteristics. Thermodynamic properties, evaluated via the quasi-harmonic Debye model, indicate that both materials maintain structural integrity up to 1200 K and 20 GPa, with ZnY_2O_4 showing superior thermal stability. Optical analyses reveal strong ultraviolet absorption, high transparency in the visible range, and low reflectivity, positioning these materials as promising candidates for UV optoelectronic applications, including UV filters, transparent conductive coatings, and window layers in tandem solar cells. The results highlight that cation substitution at the A-site (Cd^{2+} versus Zn^{2+}) significantly influences the mechanical, thermal, and optical properties, making CdY_2O_4 and ZnY_2O_4 attractive for next-generation photovoltaic and photonic devices.

Keywords: Spinel compounds; semiconductors; optical properties; thermodynamic properties; FP-LAPW.

DOI: https://doi.org/10.31349/RevMexFis.71.051002

1. Introduction

Spinel oxides, with the general formula AB_2O_4, are a widely studied class of materials due to their exceptional physical and chemical properties. These include high thermal stability, excellent mechanical strength, low dielectric losses, and strong resistance to chemical degradation at elevated temperatures [1, 2]. Crystallographically, spinels typically adopt a cubic structure (space group $Fd\bar{3}m$) with a unit cell consisting of eight formula units, incorporating 24 cations and 32 oxygen atoms. Depending on the distribution of the cations, spinels can be classified as either *normal* or *inverse*. In a normal spinel, divalent A^{2+} cations occupy one-eighth of the tetrahedral (T_d) sites, while trivalent B^{3+} cations fill one-half of the octahedral (O_h) sites. Conversely, in an inverse spinel, A^{2+} cations and half of the B^{3+} cations share the octahedral sites, while the remaining B^{3+} cations occupy the tetrahedral sites. Intermediate cation distributions may also arise depending on synthesis conditions and thermodynamic stability [3, 4].

Beyond their conventional applications in ceramics, catalysis, and magnetics, spinel oxides have increasingly drawn attention for their use in optoelectronic and photovoltaic devices. Their wide band gaps, chemical inertness, and high optical transparency make them suitable candidates for transparent conducting oxides (TCOs), window layers, and UV-absorbing components in multi-junction solar cells [5–7]. Materials such as $ZnAl_2O_4$, $ZnGa_2O_4$, and Cu-based spinels have demonstrated promising properties for such applications due to their strong light-matter interactions and suitable band alignments [8–10].

Zinc-based spinels, particularly $ZnSc_2O_4$ and ZnY_2O_4, have been studied both theoretically and experimentally. Ghosh *et al.* reported that these materials exhibit direct band gaps of 3.9 eV and 3.4 eV, respectively, making them attractive for UV-sensitive optoelectronics or as wide-band-gap subcells in tandem photovoltaic architectures [11]. Furthermore, the experimental synthesis of ZnY_2O_4 using solid-state reactions has been successfully demonstrated by Wisniewski *et al.*, who also provided detailed structural analysis using X-ray diffraction and electron microscopy techniques [12].

Despite these findings, the spinel CdY_2O_4 has remained largely unexplored. Substituting Zn with Cd introduces important electronic and structural changes due to the larger ionic radius of Cd^{2+} (0.95 Å vs. 0.74 Å for Zn^{2+}) and its lower electronegativity. This substitution is hypothesized to influence the crystal field environment, reduce p-d orbital repulsion, and possibly widen the band gap. Such effects could lead to improved light absorption in the UV region and enhanced dielectric and elastic responses-both desirable traits for thin-film photovoltaic devices [13–15]. Moreover, cadmium-based oxides are recognized for their high electron mobility and tunable band structures, further justifying their consideration in solar energy conversion technologies [16].

Accordingly, this study provides a detailed first-principles investigation of the physical properties of AY_2O_4 (A = Cd, Zn) spinels using density functional theory (DFT). We systematically examine and compare their structural, magnetic, electronic, elastic, thermodynamic, and optical behaviors to assess the impact of A-site cation substitution. The objective is to determine how replacing Zn with Cd influences these properties and to evaluate their suitability for advanced optoelectronic and photovoltaic applications. Cadmium was selected due to its heavier mass, higher polarizability, and larger ionic radius (0.95 Å compared to 0.74 Å for Zn^{2+}), as well as its 4d orbital configuration. These characteristics are expected to modify the crystal field environment and bonding nature, potentially enhancing UV-range optical absorption, dielectric response, and mechanical flexibility.

2. Computational Methodology

All first-principles calculations were conducted using the full-potential linearized augmented plane wave (FP-LAPW) method as implemented in the WIEN2K code [17–19], within the framework of density functional theory (DFT). The exchange-correlation effects were treated using the Perdew-Burke-Ernzerhof (PBE) functional within the generalized gradient approximation (GGA) [20]. The plane-wave cutoff parameter was set to $K_{\max} = 9.0/R_{\mathrm{MT}}$, where R_{MT} is the smallest atomic muffin-tin radius, and the charge density was expanded up to a Fourier cutoff of $G_{\max} = 14\,\mathrm{a.u.}^{-1}$. A Monkhorst-Pack $10 \times 10 \times 10$ k-point mesh was employed for Brillouin zone sampling. The energy separation between core and valence states was set at $-6\,\mathrm{Ry}$, and the self-consistent field calculations were converged to within $10^{-6}\,\mathrm{Ry}$ per formula unit.

Both normal and inverse spinel structures of AY_2O_4 ($A = \mathrm{Cd}, \mathrm{Zn}$) were considered. The normal spinel structure (space group $Fd\bar{3}m$) was modeled with A atoms at the $8a$ $(1/8, 1/8, 1/8)$ sites, Y at $16d$ $(1/2, 1/2, 1/2)$, and O at $32e$ (u, u, u), where the oxygen positional parameter u was optimized. The inverse spinel structure was constructed using the orthorhombic *Imma* space group, with atomic positions specified in Table I.

Structural relaxation was performed in two steps: first, the total energy as a function of volume was computed by varying the volume $\pm 5\%$ around the estimated equilibrium value, while fully relaxing internal atomic coordinates. These data were fitted to the Murnaghan equation of state to extract the equilibrium lattice parameter a_0, bulk modulus B_0, and its pressure derivative B' [21].

To identify the magnetic ground state, spin-polarized and non-spin-polarized (NM) calculations were performed. Local magnetic moments were initialized on A and Y atoms for ferromagnetic (FM) configurations, but in all cases, the NM state was more stable by more than $0.01\,\mathrm{eV}$ per formula unit.

TABLE I. Calculated total and local magnetic moments (μ_B) for the ferromagnetic (FM) configurations of CdY_2O_4 and ZnY_2O_4.

Compound	A (μ_B)	Y (μ_B)	O (μ_B)	Interstitial (μ_B)	Total (μ_B)
CdY_2O_4	0.000	0.00001	-0.0002	0.00014	0.00001
ZnY_2O_4	0.000	0.00001	-0.0002	0.00015	0.00001

To address the well-known underestimation of band gaps by GGA, electronic structure calculations were refined using the Tran-Blaha modified Becke-Johnson (TB-mBJ) potential [22]. These calculations were performed as single-point evaluations on GGA-optimized geometries without further relaxation, since TB-mBJ is computationally expensive and generally has minimal impact on lattice parameters. A comparison between GGA and TB-mBJ geometries showed negligible differences, justifying this approach. The TB-mBJ exchange potential was applied using the `TOT XC_MBJ` flag in WIEN2K with the default c-parameter ($c = 1.0$). Band structures, total density of states (TDOS), and partial density of states (PDOS) were computed for both $\mathrm{CdY_2O_4}$ and $\mathrm{ZnY_2O_4}$ using the same computational settings.

The investigation of the antiferromagnetic (AFM) state was based on the analysis of the ferromagnetic (FM) configuration. Magnetic moment calculations for $\mathrm{CdY_2O_4}$ and $\mathrm{ZnY_2O_4}$ revealed that both the total and atomic magnetic moments are negligible, with values close to zero (Table I). As a result, the AFM state was deemed irrelevant for further study in this work.

Elastic constants were calculated using the IRelast package [23], which applies small finite deformations to the relaxed structure and derives the elastic tensor from the resulting stress-strain relations, from which the bulk modulus B, shear modulus G, Young's modulus E, Poisson's ratio σ, and anisotropy factor A were derived. Mechanical stability was confirmed via the Born criteria ($C_{11} > 0, \quad C_{44} > 0, \quad C_{11} - C_{12} > 0, \quad$ and $\quad C_{11} + 2C_{12} > 0$) [24], and ductility was assessed through Pugh's ratio B/G.

Thermodynamic properties were computed using the quasi-harmonic Debye model as implemented in the GIBBS program [25]. Temperature- and pressure-dependent heat capacities C_V, C_P, Debye temperature θ_D, and thermal expansion coefficient α were calculated in the ranges 0-1200 K and 0-20 GPa.

All optical calculations were performed with carefully tested convergence parameters, including k-point sampling and energy cutoffs, to ensure the reliability of the computed dielectric functions. The optical properties were derived from the complex dielectric function $\varepsilon(\omega) = \varepsilon_1(\omega) + i\varepsilon_2(\omega)$, calculated using Kramers-Kronig relations and dipole matrix elements [26]. From this, the frequency-dependent refractive index $n(\omega)$, absorption coefficient $\alpha(\omega)$, reflectivity $R(\omega)$, and optical conductivity $\sigma(\omega)$ were obtained.

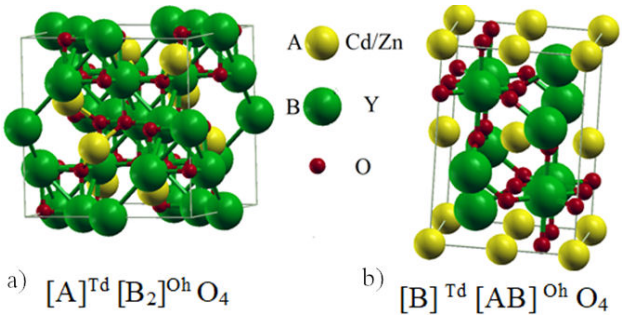

FIGURE 1. Normal and inverse spinel structures: a) Normal spinel b) inverse spinel.

3. Results and discussion

3.1. Structural properties

The structural properties of CdY_2O_4 and ZnY_2O_4 compounds were systematically investigated in both the normal and inverse spinel configurations using the generalized gradient approximation (GGA) with the Perdew–Burke–Ernzerhof (PBE) functional. In spinel structures with the general formula AB_2O_4, the O^{2-} anions form a face-centered cubic (FCC) lattice, while the A^{2+} and B^{3+} cations occupy the tetrahedral (Td) and octahedral (Oh) sites, respectively [27]. In the normal spinel structure, one-eighth of the tetrahedral sites are occupied by A^{2+} cations and half of the octahedral sites are occupied by B^{3+} cations, as illustrated in Fig. 1a) [27]. Conversely, in the inverse spinel configuration, A^{2+} and B^{3+} cations are redistributed such that they share the octahedral sites, while B^{3+} cations exclusively occupy the tetrahedral sites, as depicted in Fig. 1b) [28, 29].

These structures are formally described as $[A]_{Td}[B_2]_{Oh}O_4$ for normal spinels and $[B]_{Td}[AB]_{Oh}O_4$ for inverse spinels [28, 29]. The optimized atomic positions for CdY_2O_4 and ZnY_2O_4 are summarized in Table II. In the normal spinel phase (space group $Fd\bar{3}m$ (227)), the Cd or Zn atoms occupy the (1/8, 1/8, 1/8) positions, Y atoms are located at (1/2, 1/2, 1/2), and oxygen atoms are slightly displaced from the ideal positions, with specific coordinates close to (0.263157, 0.263157, 0.263157). In the inverse spinel structure (space group Imma (74)), a more complex atomic arrangement is observed, where Cd/Zn and Y atoms, along with O atoms, occupy multiple distinct Wyckoff sites [30–32]. For comparison, structural data from related compounds such as $CdSc_2O_4$ and $ZnSc_2O_4$, known to crystallize in the normal spinel structure, were also considered from previous studies [33].

For a more comprehensive understanding of these structures, we include a comparison with the structural data for related compounds from the literature, specifically CdY_2O_4 and ZnY_2O_4 from studies [28–33] (see Supplementary Table III). This allows for an insightful comparison of the atomic positions across various spinel compounds and provides a clearer picture of the structural variations.

In this study, the structural configurations of CdY_2O_4 and ZnY_2O_4 have been thoroughly investigated in both normal and inverse spinel forms, revealing a consistent and well-defined atomic arrangement. The calculated atomic positions align closely with those reported in previous literature. Notably, CdY_2O_4 exhibits slightly larger atomic displacements

TABLE II. Atomic positions of CdY_2O_4 and ZnY_2O_4 (This Work).

Compound	Type	Space Group	Atom	Atomic Position(s)
CdY_2O_4	Normal	$Fd\bar{3}m$ (227)	Cd	(1/8, 1/8, 1/8)
			Y	(1/2, 1/2, 1/2)
			O	(0.26134, 0.26134, 0.26134)
ZnY_2O_4	Normal	$Fd\bar{3}m$ (227)	Zn	(1/8, 1/8, 1/8)
			Y	(1/2, 1/2, 1/2)
			O	(0.26245, 0.26245, 0.26245)
CdY_2O_4	Inverse	Imma (74)	Y(1)	(0, 0.75, 0.625), (0, 0.25, 0.375)
			A	(0, 1/2, 0), (0, 0, 0)
			Y(2)	(3/4, 3/7, 1/4), (3/4, 1/4, 3/4)
			O(1)	(0, 0.01, 0.755), (0, 0.99, 0.245), (0.51, 0.245), etc.
			O(2)	(0.74, 0.75, 0.755), (0, 0.99, 0.245), etc.
ZnY_2O_4	Inverse	Imma (74)	Y(1)	(0, 0.75, 0.625), (0, 0.25, 0.375)
			A	(0, 1/2, 0), (0, 0, 0)
			Y(2)	(3/4, 3/7, 1/4), (3/4, 1/4, 3/4)
			O(1)	(0, 0.01, 0.755), (0, 0.99, 0.245), (0.51, 0.245), etc.
			O(2)	(0.74, 0.75, 0.755), (0, 0.99, 0.245), etc.

TABLE III. Comparison of atomic positions for CdY_2O_4 and ZnY_2O_4.

Compound	Type	Space Group	Atom	Atomic Position(s)	Reference
CdY_2O_4	Normal	Fd$\bar{3}$m (227)	Cd	(1/8, 1/8, 1/8)	[28]
			Y	(1/2, 1/2, 1/2)	[28]
			O	(0.263157, 0.263157, 0.263157)	[28]
ZnY_2O_4	Normal	Fd$\bar{3}$m (227)	Zn	(1/8, 1/8, 1/8)	[28]
			Y	(1/2, 1/2, 1/2)	[28]
			O	(0.26245, 0.26245, 0.26245)	This work
CdY_2O_4	Inverse	Imma (74)	Y(1)	(0, 0.75, 0.625), (0, 0.25, 0.375)	[30, 31]
			A	(0, 1/2, 0), (0, 0, 0)	[30, 31]
			Y(2)	(3/4, 3/7, 1/4), (3/4, 1/4, 3/4)	[30, 31]
			O(1)	(0, 0.01, 0.755), (0, 0.99, 0.245), (0.51, 0.245), etc.	[30, 31]
			O(2)	(0.74, 0.75, 0.755), (0, 0.99, 0.245), etc.	[30, 31]
ZnY_2O_4	Inverse	Imma (74)	Y(1)	(0, 0.75, 0.625), (0, 0.25, 0.375)	[30, 31]
			A	(0, 1/2, 0), (0, 0, 0)	[30, 31]
			Y(2)	(3/4, 3/7, 1/4), (3/4, 1/4, 3/4)	[30, 31]
			O(1)	(0, 0.01, 0.755), (0, 0.99, 0.245), (0.51, 0.245), etc.	[30, 31]
			O(2)	(0.74, 0.75, 0.755), (0, 0.99, 0.245), etc.	[30, 31]

compared to ZnY_2O_4, which can be attributed to the difference in ionic radii between Cd^{2+} and Zn^{2+} ions. Structural data for $CdSc_2O_4$ and $ZnSc_2O_4$, as reported in Ref. [33], which are known to crystallize in the normal spinel structure, further support these observations and offer a meaningful basis for comparison.

The consistency between the present results and prior studies reinforces the validity of the computational methodology employed. Minor discrepancies in atomic positions may arise from differences in computational models, temperature conditions, or refinement techniques used in various studies. Furthermore, total energy versus volume (E–V) curves were computed for both ferromagnetic (FM) and non-magnetic (NM) configurations of CdY_2O_4 and ZnY_2O_4. These curves were fitted using the Murnaghan equation of state [34] Eq. (1) to determine the equilibrium structural parameters.

$$E(V) = E_0 + \frac{B_0 V}{B'(B'-1)} \times \left[B\left(1 - \frac{V_0}{V}\right) + \left(\frac{V_0}{V}\right)^{B'} - 1 \right]. \quad (1)$$

Substituting cadmium (Cd) with zinc (Zn) in the spinel oxide CdY_2O_4 to form ZnY_2O_4 induces significant modifications in structural parameters and thermodynamic properties, primarily due to the disparity in ionic radii and bonding characteristics between Cd^{2+} and Zn^{2+} ions.

In the normal spinel configuration (space group Fd$\bar{3}$m), CdY_2O_4 exhibits a lattice constant of 9.57 Å, whereas ZnY_2O_4 has a slightly smaller lattice constant of 9.41 Å. This reduction of 0.16 Å is attributed to the smaller ionic radius of Zn^{2+} (0.74 Å) compared to Cd^{2+} (0.95 Å), leading to a more compact crystal structure. Additionally, ZnY_2O_4 demonstrates a higher bulk modulus of 146.92 GPa, indicating greater mechanical stiffness relative to CdY_2O_4, which has a bulk modulus of 127.22 GPa. The increase of approximately 19.7 GPa in bulk modulus reflects the enhanced resistance to volume compression in ZnY_2O_4. These findings align with previously reported theoretical values for ZnY_2O_4, which indicate a bulk modulus of 137.40 GPa, further validating the computational results [35].

Analysis of the total energy versus volume (E–V) curves, as presented in Figs. 2 and 3, reveals that both CdY_2O_4 and ZnY_2O_4 favor the non-magnetic normal spinel configuration as the energetically most stable phase. This observation

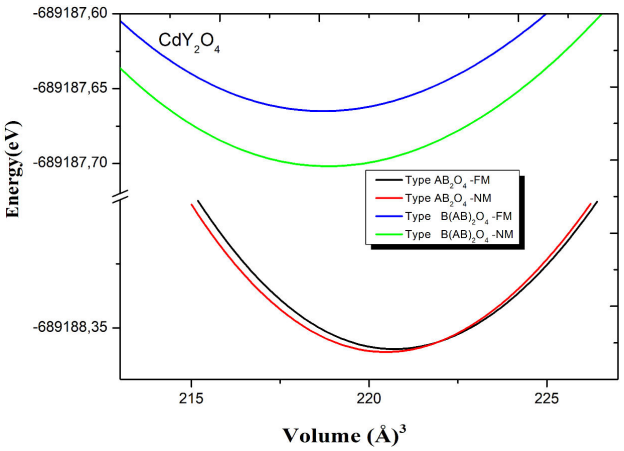

FIGURE 2. Variation of the total energy E_{tot} versus the unit cell volume for CdY_2O_4.

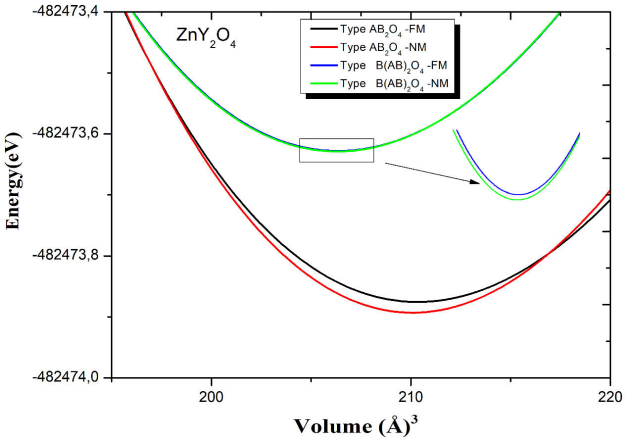

FIGURE 3. Variation of the total energy E_{tot} versus the unit cell volume for ZnY_2O_4.

aligns with the computed results summarized in Table IV, which indicate lower total energies for the non-magnetic configurations compared to their ferromagnetic counterparts. The preference for the non-magnetic phase suggests that magnetic ordering does not significantly contribute to the stabilization of these compounds.

The thermodynamic stability of CdY_2O_4 and ZnY_2O_4 was evaluated through the calculation of their formation energies using first-principles total energy data. The formation energy per atom was determined using the following expression:

$$\Delta H_f = \frac{E_0^{\mathrm{CdY_2O_4/ZnY_2}O_4} - E_0^{\mathrm{Cd/Zn}} - 2E_0^{\mathrm{Y}} - 4E_0^{\mathrm{O}}}{7}, \quad (2)$$

where $E_{\mathrm{AY_2O_4}}$ is the total DFT energy of the compound (A = Cd, Zn), and E_{0A}, E_{0Y}, and E_{0O_2} are the total energies of elemental Cd or Zn, Y, and O_2 molecule, respectively. The factor 1/7 accounts for the number of atoms in a single formula unit of AY_2O_4. Oxygen is referenced to half the energy of an isolated O_2 molecule, consistent with standard DFT conventions.

The calculated formation energies per atom are presented in Table IV. The values obtained are -9.72 eV/atom for CdY_2O_4 and -9.68 eV/atom for ZnY_2O_4. These negative values confirm the thermodynamic stability of both compounds. For comparison, the formation energy of $CdSc_2O_4$ reported in reference [33] is -5.74 eV/atom, indicating that both CdY_2O_4 and ZnY_2O_4 are significantly more stable in terms of thermodynamic formation energy. This difference may arise from the stronger bonding or electronic environment associated with the Y cation in comparison to Sc.

A direct comparison between CdY_2O_4 and ZnY_2O_4 shows that both compounds are structurally and thermodynamically stable, with very similar formation energies, indicating comparable thermodynamic feasibility. However, ZnY_2O_4 displays a higher bulk modulus (146.92 GPa vs. 127.22 GPa), suggesting it is mechanically stiffer and more resistant to compression. This reflects a typical trade-off between thermodynamic and mechanical stability when substituting larger cations (Cd^{2+}) with smaller ones (Zn^{2+}) at the A-site. The more compact ZnY_2O_4 structure benefits from tighter atomic packing, leading to improved mechanical properties, while CdY_2O_4 slightly favors energy minimization from a thermodynamic perspective. These insights are important for guiding material selection in applications where mechanical strength, thermal stability, and ease of synthesis are critical.

3.2. Electronic properties

The electronic structure of AY_2O_4 (A = Cd, Zn) spinel compounds was systematically investigated using density functional theory (DFT) with both the GGA-PBE and the more advanced Tran-Blaha modified Becke-Johnson (TB-mBJ) exchange-correlation functionals. Band structure calculations (Figs. 4 and 5) reveal that both CdY_2O_4 and ZnY_2O_4 are direct band gap semiconductors, with the con-

TABLE IV. Calculated equilibrium lattice constant (a), bulk modulus (B), total energy (E_0), and formation energy per atom (ΔH_f) for CdY_2O_4 and ZnY_2O_4 compounds, compared with available theoretical data.

Compound	Type	Phase	a (Å)	b (Å)	c/a	V_0 (Å^3)	B (GPa)	B'	E_0 (eV)	ΔH_f (eV/atom)
CdY_2O_4	Normal	FM	9.57	9.57	1	220.48	127.01	4.21	-689188.95409	
		NM	9.57	9.57	1	220.47	127.22	4.17	-689188.95421	-9.72
	Inverse	FM	8.52	8.52		218.70	123.32	5.60	-689187.66495	
		NM	8.53	8.53		218.84	128.73	4.34	-689187.70178	
$CdSc_2O_4$ [33]	Normal	NM	9.04	9.04	1		151.7	4.01		-5.74
ZnY_2O_4	Normal	FM	9.42	9.42	1	210.40	131.58	4.25	-482473.87567	-9.68
		NM	9.41	9.41	1	210.08	146.92	3.07	-482473.89309	
	Inverse	FM	8.36	8.36		206.26	132.32	3.76	-482473.62793	
		NM	8.36	8.36		206.30	132.71	3.96	-482473.63008	
ZnY_2O_4 [35]	Normal	NM	9.39	9.39	1		137.40			

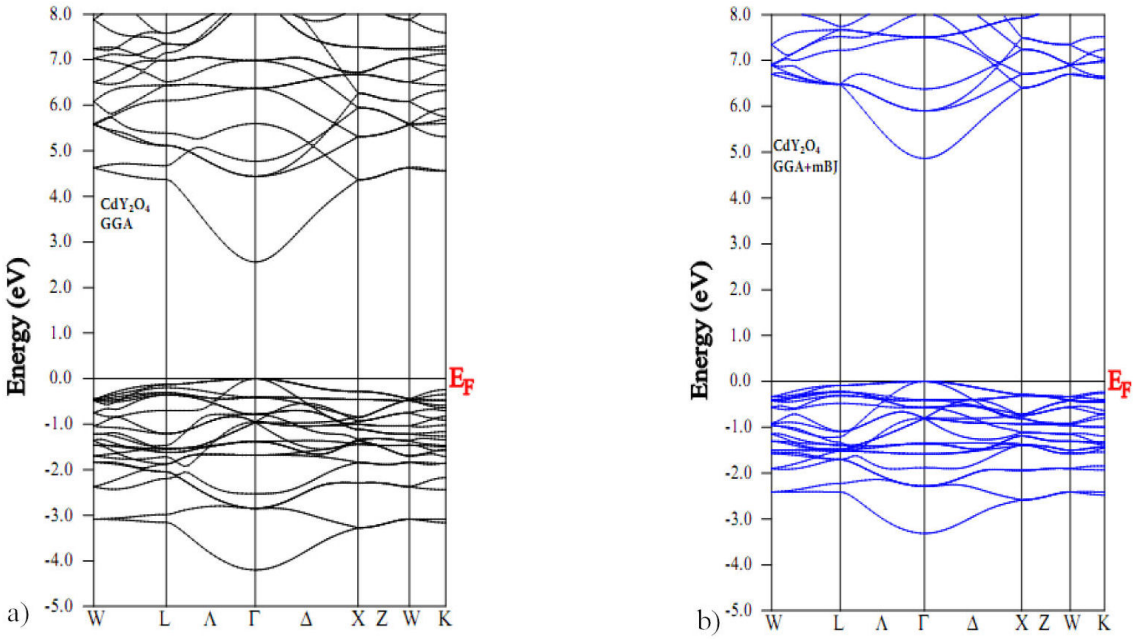

FIGURE 4. The band structures of CdY_2O_4 calculated by a) GGA and b) TB-mBJ.

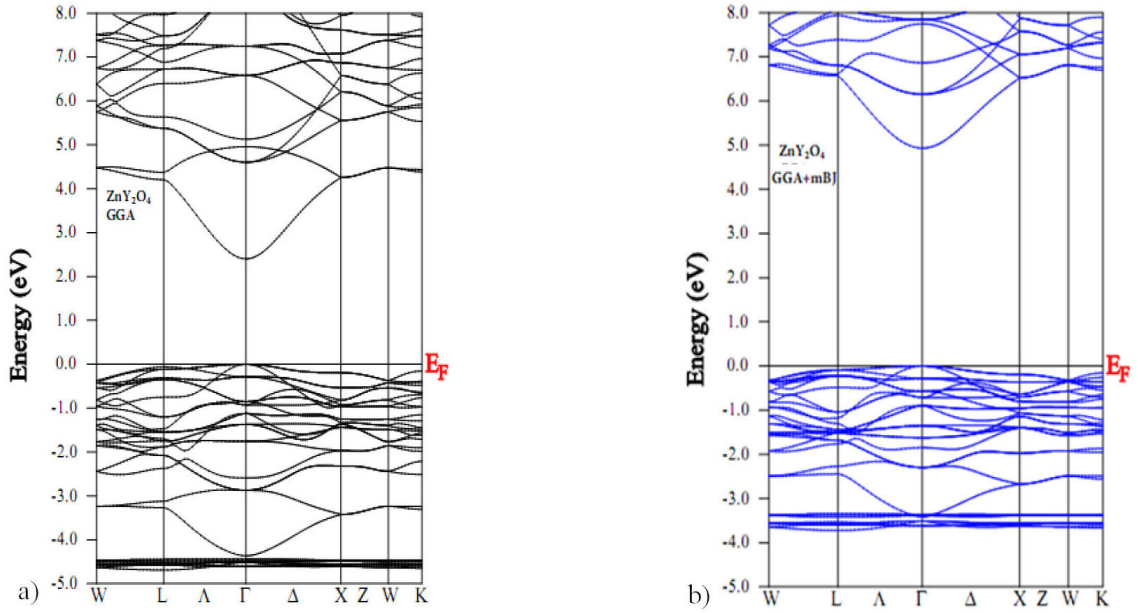

FIGURE 5. The band structures of ZnY_2O_4 calculated by a) GGA and b) TB-mBJ.

duction band minimum (CBM) and valence band maximum (VBM) located at the Γ point. The calculated band gap values are 2.55 eV (GGA) and 4.93 eV (TB-mBJ) for CdY_2O_4, and 2.40 eV (GGA) and 4.86 eV (TB-mBJ) for ZnY_2O_4 (Table V), with the TB-mBJ functional providing a more accurate description of the electronic structure due to its improved treatment of the exchange potential. Although both compounds exhibit well-defined semiconducting behavior, their TB-mBJ-corrected band gaps are significantly wider than the ideal range (1.1-1.6 eV) for efficient visible light absorption, rendering them unsuitable as primary absorber layers in single-junction solar photovoltaic cells. In comparison to commercial solar absorber materials such as silicon (1.1 eV), CdTe (1.5 eV), and hybrid perovskites (∼1.6 eV) [36], the large band gaps of AY_2O_4 highlight their limited applicability for traditional photovoltaic devices.

Nevertheless, their wide band gaps and high optical transparency (as we will see in the optical properties later) suggest potential for alternative applications, including ultraviolet (UV) light-emitting diodes (LEDs), transparent conducting oxides (TCOs), UV photodetectors, and wide-band-gap buffer layers in tandem solar cells. A slight reduction in the

TABLE V. Band gap E_g (eV) of AY_2O_4 (A = Cd, Zn) calculated by GGA and GGA+mBJ approximations.

Compounds	E_g (eV) (GGA)	E_g (eV) (GGA+mBJ)
CdY_2O_4	2.55	4.93
ZnY_2O_4	2.40	4.86
	Other Work	
ZnY_2O_4		3.4 [35] (TB-LMTOs)

in the band gap is observed when substituting Cd with Zn, attributable to differences in electronic configuration, orbital characteristics, and bonding environments. Specifically, Zn^{2+}, with its more localized 3*d* orbitals compared to the delocalized 4*d* orbitals of Cd^{2+}, leads to reduced hybridization with O 2*p* orbitals, stronger Zn-O covalency, and subtle modifications of the crystal field environment due to the smaller ionic radius of Zn. These factors collectively influence the splitting and energy alignment of the *d*-orbital states, resulting in a narrowed band gap in ZnY_2O_4 relative to CdY_2O_4. Density of states (DOS) analysis (Figs. 6 and 7) further supports these findings, showing that the valence band is primarily composed of O 2*p* and Cd/Zn *d* states, while the conduction band is dominated by Y 4*d* states with minor O 2*p* contributions. The substitutional effect of Cd by Zn also leads to a slight reduction in the intensity and energy spread of the *d*-states due to the differing spatial extent and energy levels of the 3*d* versus 4*d* orbitals. Overall, these results highlight the strong sensitivity of the electronic properties of AY_2O_4 compounds to the choice of A-site cation, underscoring the importance of employing accurate exchange-correlation approximations for reliable electronic structure predictions and suggesting promising opportunities for their use in advanced optoelectronic and photonic applications.

3.3. Elastic properties

The elastic constants characterize a crystal's ability to resist external stresses and are typically determined using approaches such as the volume conservation method and the stress-strain method [37–40]. In the present work, we applied the volume conservation method to calculate the elastic constants (C_{11}, C_{12}, and C_{44}) for the cubic CdY_2O_4 and ZnY_2O_4 compounds. These constants were then utilized to derive key mechanical parameters, including the shear modulus G, Young's modulus E, and Poisson's ratio σ, based on the standard expressions [41–43]:

$$E = \frac{9BG}{3B+G}, \tag{3}$$

$$C = \frac{(C_{11} - C_{12} - 3C_{44})}{5}, \tag{4}$$

$$\sigma = \frac{(3B - 2G)}{2(3B+G)}, \tag{5}$$

$$A = \frac{(2C_{44} + C_{12})}{C_{11}}. \tag{6}$$

Mechanical stability was verified by applying the Born stability criteria for cubic crystals, which require that ($C_{11} > 0$, $C_{44} > 0$, $C_{11} - C_{12} > 0$, and $C_{11} + 2C_{12} > 0$) [44] (see Table VI). Furthermore, in both materials, C_{11} is greater than C_{44}, indicating a lower resistance to shear deformation. To

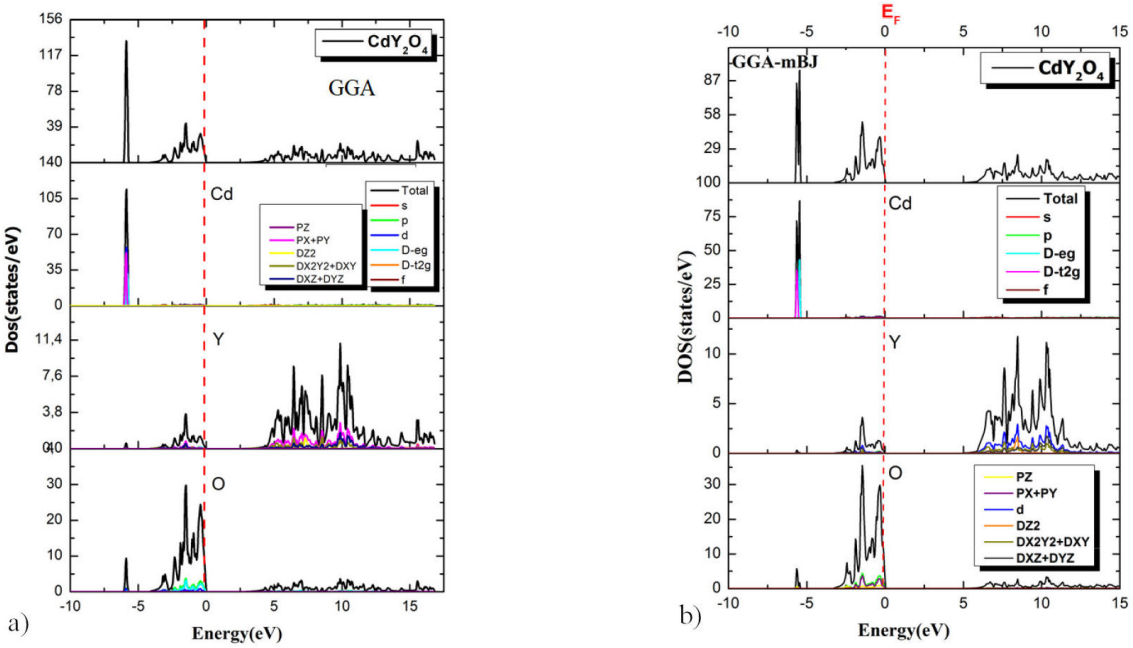

FIGURE 6. Total and partial density of states for CdY_2O_4 with GGA a) and GGA-mBJ b).

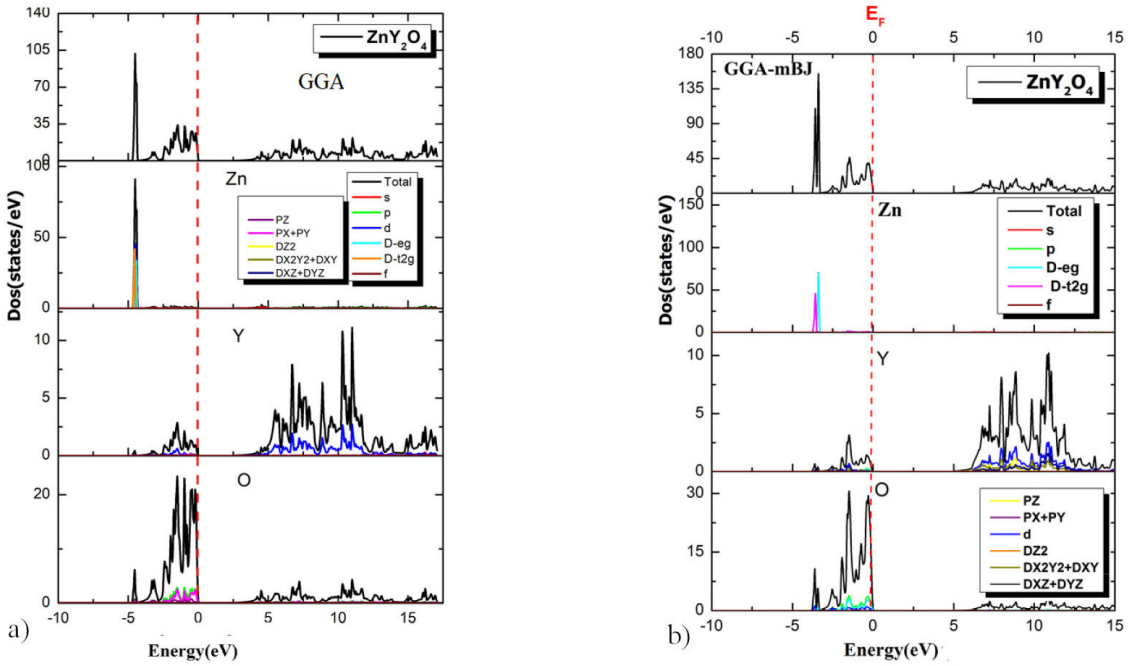

FIGURE 7. Total and partial density of states for ZnY_2O_4 with GGA a) and GGA-mBJ b).

To evaluate the elastic anisotropy, the anisotropy factor A was calculated [45], with values of 0.65 for CdY_2O_4 and 0.36 for ZnY_2O_4, demonstrating that both compounds are anisotropic, with anisotropy increasing after substituting Cd with Zn.

The substitution of Cd by Zn leads to noticeable enhancements in the elastic behavior: ZnY_2O_4 shows higher values of C_{11} (315.95 GPa) and bulk modulus B (146.98 GPa) compared to CdY_2O_4 ($C_{11} = 248.96$ GPa, $B = 127.75$ GPa), indicating greater stiffness and resistance to volume compression. Additionally, both G and E increase upon Zn substitution, highlighting improved mechanical rigidity. However, according to Pugh's criterion [46], the B/G ratio drops from 1.77 (CdY_2O_4) to 1.72 (ZnY_2O_4), suggesting that while CdY_2O_4 behaves ductilely, ZnY_2O_4 becomes slightly more brittle. This brittleness in ZnY_2O_4 aligns with its increased elastic anisotropy.

The Poisson's ratio σ was also evaluated, yielding 0.26 for CdY_2O_4 and 0.25 for ZnY_2O_4, indicating that both materials are incompressible. Furthermore, the higher bulk modulus of ZnY_2O_4 implies superior hardness compared to CdY_2O_4 [47]. Overall, the substitution of Cd by Zn enhances the mechanical strength, hardness, and stiffness of the spinel structure, though at the expense of increased anisotropy and a modest shift toward brittleness. Further investigation of elastic anisotropy through the directional dependence of Young's modulus, using visualization tools such as VELAS or ELATE, is planned for future work.

TABLE VI. Values of the anisotropy parameter A, the elastic constants C_{ij} (GPa), the bulk modulus B (GPa), the shear modulus G (GPa), the Young's modulus E (GPa), and sound velocities v_s, v_l, and v_m (m/s) for the compounds AY_2O_4 (A = Cd, Zn).

Property	**CdY_2O_4**	**ZnY_2O_4**
B (GPa)	127.75	146.98
C_{11} (GPa)	248.96	315.95
C_{12} (GPa)	67.085	39.31
C_{44} (GPa)	59.265	50.07
G (GPa)	71.93	85.37
E (GPa)	181.69	214.55
A	0.65	0.36
v_s (m/s)	3684.07	4182.56
v_l (m/s)	6496.17	7309.69
v_m (m/s)	4096.29	4647.05

3.4. Thermodynamic properties

The thermodynamic behavior of the CdY_2O_4 and ZnY_2O_4 spinel compounds was thoroughly investigated using the quasi-harmonic Debye model, implemented via the GIBBS program [48], across a temperature range of 0–1200 K and a pressure range of 0–20 GPa. According to dynamical principles, when the lattice temperature exceeds absolute zero, the lattice energy fluctuates around a mean value due to random atomic vibrations, which are quantized as phonons. These thermal phonons significantly influence the thermal, electrical, and mechanical properties of solids. The Debye quasi-harmonic model, initially proposed by Debye [49] and consistent with Dulong–Petit's law at high temperatures [50], successfully captures the phonon contributions to thermodynamic properties.

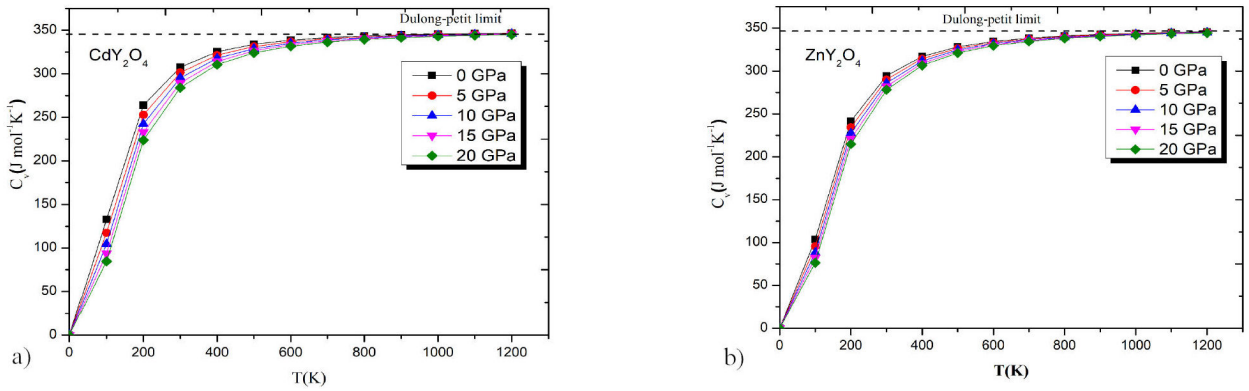

FIGURE 8. Variation of the specific heat at constant volume (C_v) with temperature at selected pressures for CdY_2O_4 and ZnY_2O_4 alloys.

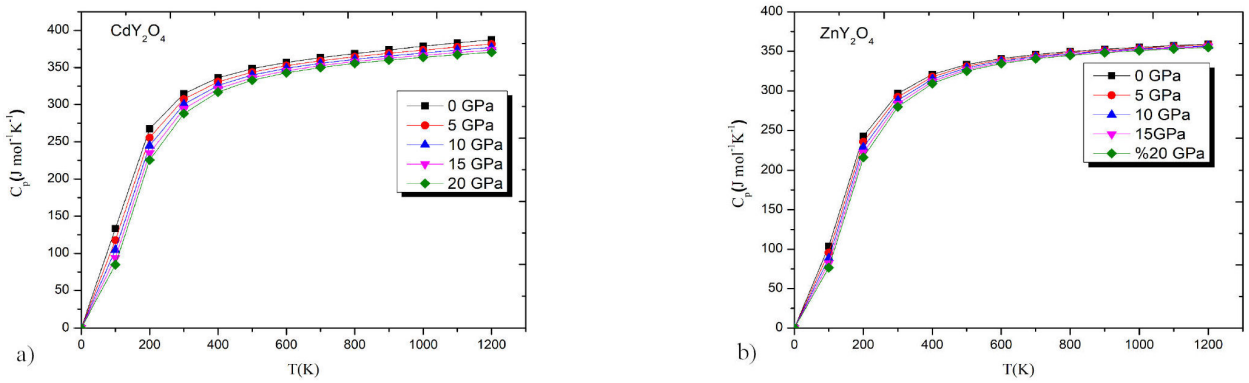

FIGURE 9. Variation of the specific heat at constant pressure (C_p) with temperature at selected pressures for CdY_2O_4 and ZnY_2O_4 alloys.

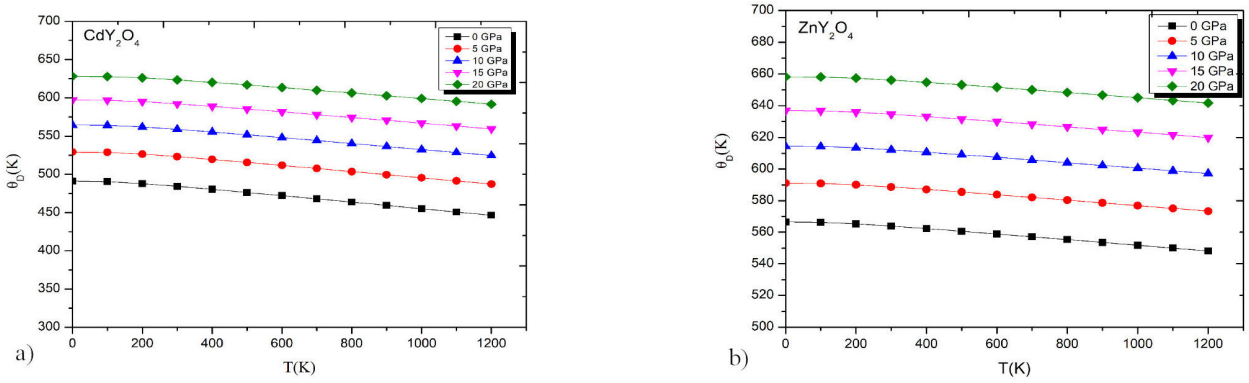

FIGURE 10. Variation of the Debye temperature (θ_D) with temperature at selected pressures for CdY_2O_4 and ZnY_2O_4 alloys.

In this study, key thermodynamic quantities, including the specific heat capacities at constant volume (C_v) and pressure (C_p), Debye temperature (Θ_D), and thermal expansion coefficient (α), were calculated. As shown in Figs. 8 and 9, $C_v(T)$ and $C_p(T)$ curves start from zero at 0 K and increase rapidly with temperature, reaching approximately 300 J/mol·K around 700–800 K, consistent with the Dulong–Petit limit [51]. Notably, while C_v tends to saturate at high temperatures, C_p decreases under pressure above 700 K, highlighting the effect of phonon softening under compression.

The Debye temperatures at 0 GPa were determined to be 480 K for CdY_2O_4 and 575 K for ZnY_2O_4 (Fig. 10), indicating that Zn substitution enhances the lattice stiffness and thermal stability. Furthermore, the Debye temperature decreases with rising temperature, reflecting the anharmonic behavior typical of solid materials.

Thermal expansion behavior, depicted in Fig. 11, reveals that at low temperatures, the thermal expansion coefficient α increases exponentially, becoming almost linear beyond 400 K. At 500 K and 0 GPa, α values are 4.2×10^{-5} K^{-1} for CdY_2O_4 and 2.37×10^{-5} K^{-1} for ZnY_2O_4, respectively.

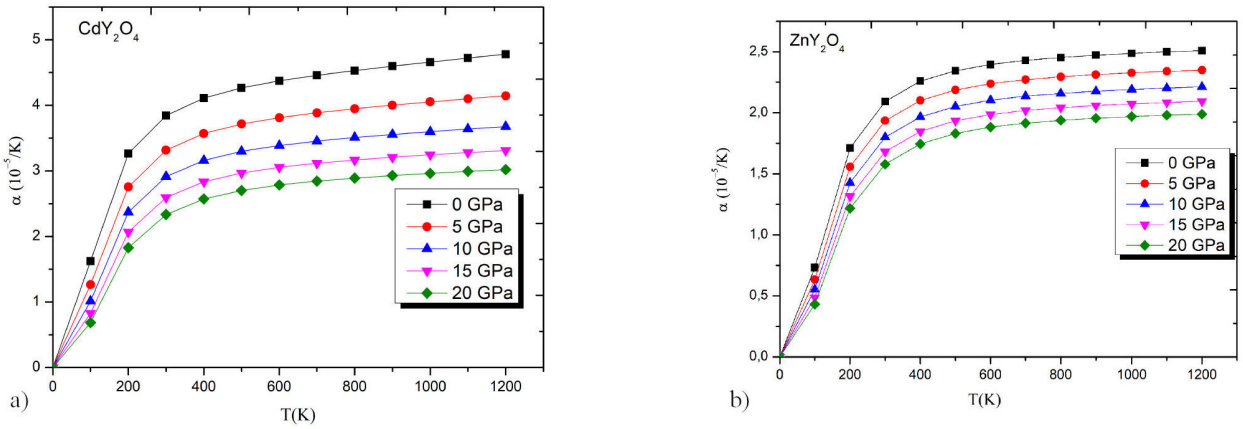

FIGURE 11. Variation of the thermal expansion coefficient (α) with temperature at selected pressures for CdY_2O_4 and ZnY_2O_4 alloys.

These results suggest that ZnY_2O_4 exhibits less thermal expansion and greater structural rigidity compared to CdY_2O_4. Importantly, both compounds retain mechanical and thermal stability up to 1200 K and under pressures up to 20 GPa, making them promising candidates for applications in high-temperature and high-pressure environments.

Overall, the substitution of Cd by Zn significantly improves the thermal stability, stiffness, and resistance to thermal deformation of the material, as evidenced by higher Debye temperatures, lower thermal expansion coefficients, and more robust thermodynamic behavior under varying temperature and pressure conditions.

3.5. Optical properties

The optical properties of solids play a critical role in materials research. A comprehensive understanding of these properties is essential for improving photonic devices used in optical communication [52]. The complex dielectric function is the key variable in calculating optical properties, as indicated in Eq. (7):

$$\varepsilon(\omega) = \varepsilon_1(\omega) + i\varepsilon_2(\omega). \tag{7}$$

The real component of the dielectric function is obtained from its imaginary part through the Kramers-Kronig relations [53]. Simultaneously, the imaginary part is calculated using the methods described in reference [53]. The real component, denoted as $\varepsilon_1(\omega)$, is evaluated using the Cauchy principal value integral p with the following equation:

$$\varepsilon_1(\omega) = 1 + \frac{2}{\pi} P \int_0^{\infty} \frac{\varepsilon_2(\omega')\,\omega'}{\omega'^2 - \omega^2} d\omega', \tag{8}$$

where p is the principal value of the Cauchy integral and ω is the frequency. The imaginary component, $\varepsilon_2(\omega)$, is determined as follows:

$$\varepsilon_2(\omega) = \frac{e^2 h}{\pi \omega^2 m^2} \sum_{v,c} \int_{BZ} |M_{cv}(k)|^2 \delta(\omega_{cv} - \omega) d^3k, \tag{9}$$

where $\mathbf{k}$ represents the irreducible wave vector in the first Brillouin zone (BZ), $M_{cv}(\mathbf{k}) = \langle u_{c\mathbf{k}} | \mathbf{e} \cdot \nabla | u_{v\mathbf{k}} \rangle$ denotes the elements of the dipole moment matrix for direct transitions between the valence band $u_{v\mathbf{k}}$ and the conduction band $u_{c\mathbf{k}}$. $\mathbf{e}$ is the polarization vector defining the electric field, and $\hbar\omega_{cv} = E_c(\mathbf{k}) - E_v(\mathbf{k})$ corresponds to the respective transition energy. Other important optical constants, including the refractive index $n(\omega)$, absorption coefficient $\alpha(\omega)$, reflectivity $R(\omega)$, and optical conductivity $\sigma(\omega)$, are calculated using the functions $\varepsilon_1(\omega)$ and $\varepsilon_2(\omega)$, based on the equations outlined in references [54–57].

The optical properties of CdY_2O_4 and ZnY_2O_4 spinel compounds were comprehensively investigated based on electronic structures calculated using the TB-mBJ potential, with detailed results presented in Figs. 12- 17 and Tables VII and VIII. Both materials exhibit excellent transparency in the visible region and strong optical activity in the ultraviolet (UV) range. Their low static dielectric constants (~ 2.521

TABLE VII. Values of static constants of the real part of dielectric constant $\varepsilon_1(0)$, refractive index $n(0)$, and reflectivity $R(0)$ for CdY_2O_4 and ZnY_2O_4.

Parameters	CdY_2O_4	ZnY_2O_4
$\varepsilon_1(0)$	2.52104	2.52497
$n(0)$	1.58778	1.58902
$R(0)$	0.05159	0.05176

TABLE VIII. Positions of the peaks of $\varepsilon_1(\omega)$, $\varepsilon_2(\omega)$, $n(\omega)$, $\alpha(\omega)$, and $\sigma(\omega)$ for CdY_2O_4 and ZnY_2O_4 (in eV).

Function	CdY_2O_4 Peaks (eV)	ZnY_2O_4 Peaks (eV)
$\varepsilon_1(\omega)$	6.47, 9.00	6.70, 9.39
$\varepsilon_2(\omega)$	4.56, 6.92, 10.75	4.80, 7.16, 10.95
$n(\omega)$	6.54, 9.07	6.79, 9.44
$\alpha(\omega)$	4.56, 7.67, 10.92	4.80, 7.48, 11.37
$\sigma(\omega)$	4.56, 7.00, 10.70	4.80, 7.16, 11.05

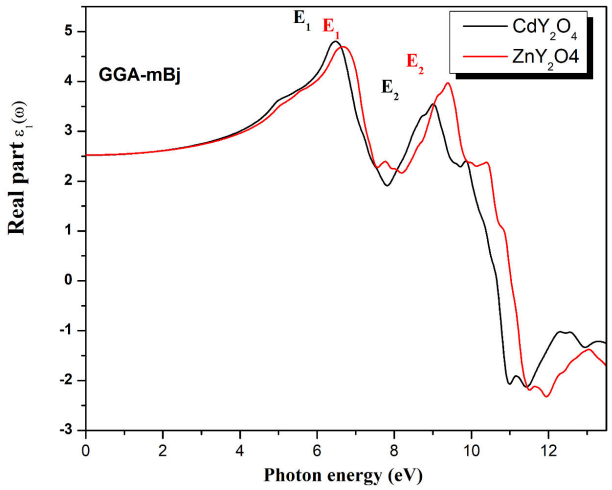

FIGURE 12. The real part of dielectric function of CdY_2O_4 and ZnY_2O_4 compounds calculated by TB-mBJ.

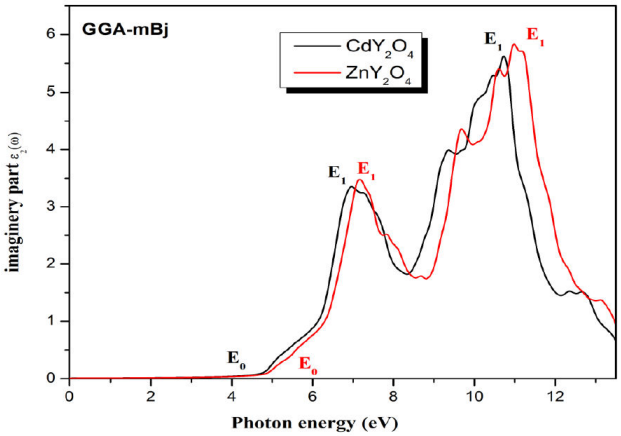

FIGURE 13. The imaginary part of dielectric function of CdY_2O_4 and ZnY_2O_4 compounds calculated by TB-mBJ.

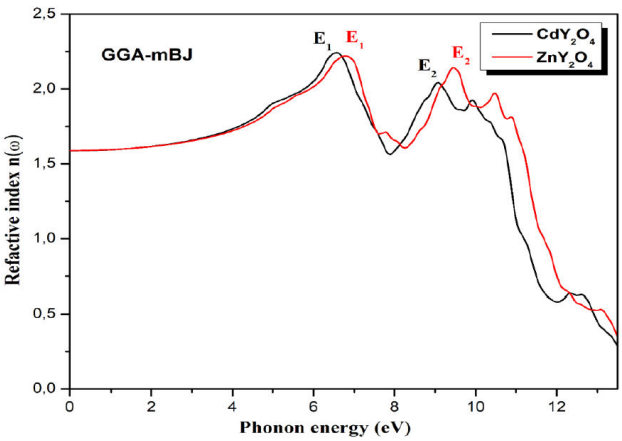

FIGURE 14. The refractive index $n(\omega)$ of CdY_2O_4 and ZnY_2O_4 compounds calculated by TB-mBJ.

for CdY_2O_4 and ~ 2.525 for ZnY_2O_4) and refractive indices ($\sim$ 1.588-1.589) indicate weak polarizability and minimal light interaction at low photon energies. These low permittivity values also reflect weak polarization under external electric fields.

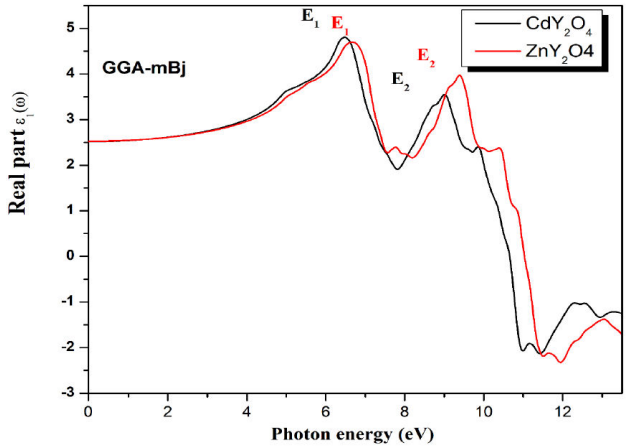

FIGURE 15. The absorption coefficient of CdY_2O_4 and ZnY_2O_4 compounds calculated by TB-mBJ.

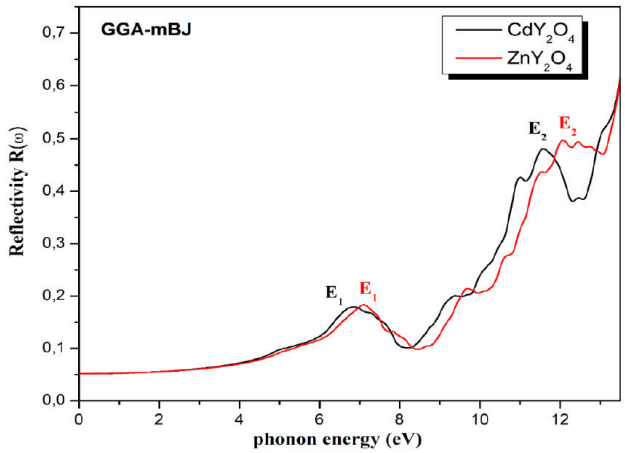

FIGURE 16. The reflectivity of CdY_2O_4 and ZnY_2O_4 compounds calculated by TB-mBJ

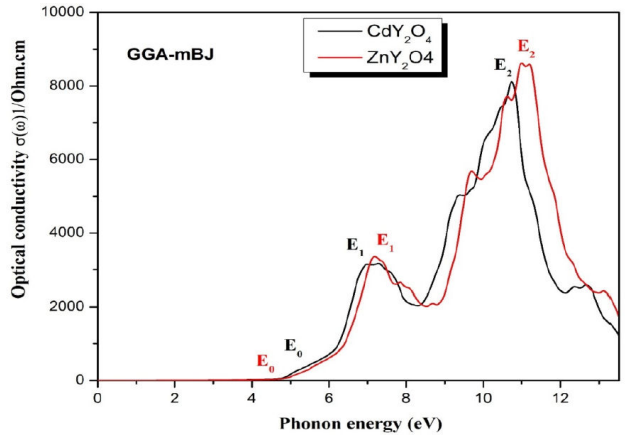

FIGURE 17. The optical conductivity of CdY_2O_4 and ZnY_2O_4 compounds calculated by TB-mBJ.

Substituting Cd with Zn results in a slight increase in both the static dielectric constant and refractive index, suggesting marginally enhanced electronic polarization due to Zn's smaller atomic radius and stronger bonding. The real part of the dielectric function, $\varepsilon_1(\omega)$, shows a resonance peak at

6.47 eV for CdY_2O_4 and shifts to 6.70 eV for ZnY_2O_4, indicating an upward shift in resonant transition energy. At higher photon energies ($\sim$ 10.8-13.5 eV), $\varepsilon_1(\omega)$ becomes negative for both materials, implying a plasmonic-like response, which correlates with peaks observed in the reflectivity spectra (Fig. 16).

The imaginary part, $\varepsilon_2(\omega)$, reveals absorption edges at 4.56 eV (CdY_2O_4) and 4.80 eV (ZnY_2O_4), consistent with the electronic band gaps obtained from TB-mBJ calculations. These thresholds mark the onset of strong absorption ($\alpha(\omega) > 10^4\,\mathrm{cm}^{-1}$), with several sharp peaks at higher energies attributed to interband electronic transitions. The refractive index, $n(\omega)$, reaches its maximum near 6.5-6.8 eV, consistent with the dielectric behavior, while reflectivity increases in the UV region due to the negative values of $\varepsilon_1(\omega)$. Optical conductivity, $\sigma(\omega)$, which represents the real part of the frequency-dependent conductivity arising from photon-induced electronic transitions, begins at the absorption edge and peaks at $\sim$ 10.70 eV for CdY_2O_4 and $\sim$ 11.05 eV for ZnY_2O_4, indicating stronger UV-driven carrier excitation in Zn-based compounds. Although the extinction coefficient was not plotted in this work, it will be included in future studies for a more complete optical characterization.

Overall, ZnY_2O_4 demonstrates slightly higher critical points in all optical functions-absorption, conductivity, and dielectric response-compared to CdY_2O_4. This reflects stiffer electronic transitions and a wider band gap, attributed to Zn's stronger interatomic interactions. The substitution of Cd with Zn therefore shifts optical responses to higher photon energies, enhances excitation thresholds, and maintains excellent UV absorption alongside visible transparency. These features make both materials promising for UV optoelectronic applications, with ZnY_2O_4 being particularly well-suited for deep-UV technologies such as UV filters, transparent conductive coatings, UV-protective layers, window layers in tandem solar cells, and UV photodetectors.

4. Conclusion

In this work, a detailed first-principles study of the spinel compounds CdY_2O_4 and ZnY_2O_4 was carried out using the FP-LAPW method with the GGA-PBE and TB-mBJ exchange-correlation functionals. Structural optimizations confirmed the nonmagnetic ground state and the stability of the normal spinel phase for both materials. Electronic structure calculations revealed that both compounds are direct band gap semiconductors, with wide band gaps suitable for UV applications but not for conventional single-junction solar absorbers. Mechanical analysis demonstrated that Zn substitution improves stiffness and hardness at the cost of increased brittleness and anisotropy. Thermodynamic properties, evaluated using the quasi-harmonic Debye model, showed excellent thermal stability up to high temperatures and pressures, with ZnY_2O_4 offering enhanced robustness. Optical property analyses indicated strong ultraviolet absorption, high transparency in the visible range, and low reflectivity, making these spinels highly suitable for UV optoelectronic devices. Overall, the findings suggest that CdY_2O_4 and ZnY_2O_4 possess a combination of desirable optical, mechanical, and thermal properties, highlighting their potential for use in photovoltaic technologies and advanced optoelectronic applications operating across the UV-visible spectrum.

1. D. S. Ginley and C. Bright, Transparent conducting oxides, *MRS Bulletin* **25** (2000) 15, https://doi.org/10.1557/mrs2000.227
2. T. Minami, Transparent conducting oxide semiconductors for transparent electrodes, *Semiconductor Science and Technology* **20** (2005) S35, https://doi.org/10.1088/0268-1242/20/4/S03
3. M. Nolan and S. D. Elliott, The p-type conduction mechanism in CuAlO2: A hybrid density functional study, *Physical Chemistry Chemical Physics* **8** (2006) 5350, https://doi.org/10.1039/B609567J
4. S. D. Mo and W. Y. Ching, Electronic and optical properties of three phases of alumina by first-principles calculations, *Physical Review B* **51** (1995) 13023, https://doi.org/10.1103/PhysRevB.51.13023
5. S. R. Pendharkar *et al.*, Spinel oxides in photovoltaics and photocatalysis, *Journal of Materials Chemistry A* **10** (2022) 10975, https://doi.org/10.1039/D2TA02138D
6. R. H. French, Electronic band structure of AlO, with comparison to AlON and AlN, *Journal of the American Ceramic Society* **73** (1990) 477, https://doi.org/10.1111/j.1151-2916.1990.tb05675.x
7. J. Robertson and S. J. Clark, Limits to doping in oxides, *Physical Review B* **83** (2011) 075205, https://doi.org/10.1103/PhysRevB.83.075205
8. S. Kim *et al.*, Electronic structure and optical properties of spinel oxides: ZnAlO and ZnGaO, *Journal of Physics: Condensed Matter* **21** (2009) 195403, https://doi.org/10.1088/0953-8984/21/19/195403
9. N. Ueda *et al.*, Transparent p-type semiconducting CuAlO thin films prepared by pulsed laser deposition, *Applied Physics Letters* **70** (1997) 3561, https://doi.org/10.1063/1.119435
10. C. H. Bhosale *et al.*, Preparation and characterization of CdO thin films by spray pyrolysis, *Materials Chemistry and Physics* **78** (2002) 122, https://doi.org/10.1016/S0254-0584(02)00352-5
11. R. Ghosh, D. Choudhury, and D. Sanyal, Electronic structure of ZnScO and ZnYO using tight-binding LMTO method, *Computational Materials Science* **38** (2007) 700, https://doi.org/10.1016/j.commatsci.2006.12.019

12. W. Wisniewski *et al.*, Solid-state synthesis and microstructural characterization of ZnYO spinel, *Journal of the European Ceramic Society* **32** (2012) 3207, https://doi.org/10.1016/j.jeurceramsoc.2012.03.015
13. A. A. Lavrentyev *et al.*, Electronic structure and optical properties of RbPbBr, *Journal of Physics and Chemistry of Solids* 91 (2016) 25, https://doi.org/10.1016/j.jpcs.2015.11.008
14. N. Ueda and H. Hosono, Electronic structure and optical band gaps of transparent p-type semiconducting oxides, *Journal of Applied Physics* **91** (2002) 4769, https://doi.org/10.1063/1.1462879
15. L. Wang, T. Maxisch, and G. Ceder, Oxidation energies of transition metal oxides within the GGA+U framework, *Physical Review B* **73** (2006) 195107, https://doi.org/10.1103/PhysRevB.73.195107
16. C. H. Bhosale *et al.*, Optical and electrical characterization of CdO thin films deposited by chemical spray pyrolysis, *Thin Solid Films* **518** (2010) 1725, https://doi.org/10.1016/j.tsf.2009.10.055
17. P. Blaha, *et al.*, WIEN2k: An Augmented Plane Wave + Local Orbitals Program for Calculating Crystal Properties, Vienna University of Technology, Austria (2001).
18. D. J. Singh and L. NordstrÃ¶m, Planewaves, Pseudopotentials, and the LAPW Method (Springer, 2006).
19. K. Schwarz, P. Blaha, and G. K. H. Madsen, Electronic structure calculations of solids using the WIEN2k package for material sciences, *Computer Physics Communications* **147** (2002) 71, https://doi.org/10.1016/S0010-4655(02)00524-4
20. J. P. Perdew, K. Burke, and M. Ernzerhof, Generalized Gradient Approximation Made Simple, *Physical Review Letters* **77** (1996) 3865, https://doi.org/10.1103/PhysRevLett.77.3865
21. F. D. Murnaghan, The compressibility of media under extreme pressures, *Proceedings of the National Academy of Sciences* **30** (1944) 244, https://doi.org/10.1073/pnas.30.9.244
22. F. Tran and P. Blaha, Accurate band gaps of semiconductors and insulators with a semilocal exchange-correlation potential, *Physical Review Letters* **102** (2009) 226401, https://doi.org/10.1103/PhysRevLett.102.226401
23. M. Jamal, *et al.*, IRelast: A tool for calculating elastic constants from first principles calculations, *Computer Physics Communications* **184** (2013) 2199, https://doi.org/10.1016/j.cpc.2013.02.010
24. M. de Jong *et al.*, Charting the complete elastic properties of inorganic crystalline compounds, Scientific Data **2** (2015) 150009, https://doi.org/10.1038/sdata.2015.9
25. M. A. Blanco, E. Francisco, and V. Luana, GIBBS: isothermal-isobaric thermodynamics of solids from energy curves using a quasi-harmonic Debye model, *Computer Physics Communications* **158** (2004) 57, https://doi.org/10.1016/j.cpc.2003.12.001
26. M. Gajdoš, *et al.*, Linear optical properties in the projectoraugmented wave methodology, *Physical Review B* **73** (2006) 045112, https://doi.org/10.1103/PhysRevB.73.045112
27. K. Bouferrache *et al.*, Electronic structure, magnetic and optic properties of spinel compound NiFeO, *Semiconductor Science and Technology* **35** (2020) 095013, https://doi.org/10.1088/1361-6641/ab9a68
28. A. H. Reshak, S. A. Khan, and Z. A. Alahmed, Investigation of electronic structure and optical properties of MgAlO: DFT approach, *Optical Materials* **37** (2014) 322, https://doi.org/10.1016/j.optmat.2014.02.008
29. L. Bao *et al.*, Atomic-scale imaging of cation ordering in inverse spinel ZnSnO nanowires, *Nano Letters* **14** (2014) 6505, https://doi.org/10.1021/nl503144k
30. M. Kim *et al.*, Corrosion protection oxide scale formed on surface of Fe-Ni-M (M= Al, Cr, Cu) inert anode for molten salt electrolysis, *Materials* **15** (2022) 719, https://doi.org/10.3390/ma15030719
31. V. G. Ivanov *et al.*, Short-range B-site ordering in the inverse spinel ferrite NiFeO, *Physical Review B* **82** (2010) 024104, https://doi.org/10.1103/PhysRevB.82.024104
32. J. Liu *et al.*, Unified view of the local cation-ordered state in inverse spinel oxides, *Inorganic Chemistr*y **58** (2019) 14389, https://doi.org/10.1021/acs.inorgchem.9b01775
33. Y. Guermit *et al.*, Theoretical investigation of the physical properties of spinel-type catalysts based on Scandium: CdScO and ZnScO, *Optical and Quantum Electronics* **56** (2024) 537, https://doi.org/10.1007/s11082-024-04588-w
34. F. D. Murnaghan, The compressibility of media under extreme pressures, *Proceedings of the National Academy of Sciences* **30** (1944) 244, https://doi.org/10.1073/pnas.30.9.244
35. A. Ghosh *et al.*, Electronic structure of spinel oxides ZnScO and ZnYO: A first principle study, *In AIP Conference Proceedings*, **1675** (2015) 010045, https://doi.org/10.1063/1.4936972.
36. M. A. Green, A. Ho-Baillie, and H. J. Snaith, The emergence of perovskite solar cells, *Nature Photonics* **8** (2014) 506, https://doi.org/10.1038/nphoton.2014.134
37. J. Mehl, Pressure dependence of the elastic moduli in aluminum-rich Al-Li compounds, *Physical Review B* **47** (1993) 2493, https://doi.org/10.1103/PhysRevB.47.2493
38. O. H. Nielsen and R. M. Martin, First-Principles Calculation of Stress, *Physical Review Letters* **50** (1983) 697, https://doi.org/10.1103/PhysRevLett.50.697
39. Y. Le Page and P. Saxe, Symmetry-general least-squares extraction of elastic data for strained materials from ab initio calculations of stress, *Physical Review B* **65** (2002) 104104, https://doi.org/10.1103/PhysRevB.65.104104
40. S. Q.Wang and H. Q. Ye, First-principles study on elastic properties and phase stability of III-V compounds, *Physica Status Solidi (b)* **240** (2003) 45, https://doi.org/10.1002/pssb.200304069

41. W. Voigt, Lehrbuch der Kristallphysik (Teubner, Leipzig, 1928), Advances in Earth Science, 1, 1-978.

42. V. Kanchana, G. Vaitheeswaran, and A. Svane, Calculated structural, elastic, and electronic properties of SrCl, *Journal of Alloys and Compounds* **455** (2008) 480, https://doi.org/10.1016/j.jallcom.2007.11.069

43. R. Terki *et al.*, Full potential calculation of structural, elastic, and electronic properties of BaZrO and SrZrO, *Physica Status Solidi (b)* 242 (2005) 1054, https://doi.org/10.1002/pssb.200445313

44. G. V. Sin'Ko and N. A. Smirnov, Ab initio calculations of elastic constants and thermodynamic properties of bcc, fcc, and hcp Al crystals under pressure, *Journal of Physics: Condensed Matter* **14** (2002) 6989, https://doi.org/10.1088/0953-8984/14/29/308

45. Y. Guermit *et al.*, Investigation of structural, elastic, electronic, magnetic and thermoelectric properties for MnRhZ (Z = Al, Si, and Ge) full-Heusler alloys, *International Journal of Thermophysics* **42** (2021) 1, https://doi.org/10.1007/s10765-021-02835-1

46. S. F. Pugh, Relations between the elastic moduli and the plastic properties of polycrystalline pure metals, *The London, Edinburgh, and Dublin Philosophical Magazine and Journal of Science* **45** (1954) 823, https://doi.org/10.1080/14786435408238134

47. J. Haines, J. M. Leger, and G. Bocquillon, Synthesis and design of superhard materials, *Annual Review of Materials Research* **31** (2001) 1, https://doi.org/10.1146/annurev.matsci.31.1.1

48. V. V. Romaka *et al.*, Determination of structural disorder in Heusler-type phases, *Computational Materials Science* **172** (2020) 109307, https://doi.org/10.1016/j.commatsci.2019.109307

49. P. Debye, Theory of specific heats, *Annalen der Physik* **39** (1912) 784, https://doi.org/10.1002/andp.19123490903

50. Y.-Q. Xia *et al.*, Recent progress in networked control systems-A survey, *International Journal of Automation and Computing* **12** (2015) 343, https://doi.org/10.1007/s11633-015-0914-2

51. A. M. Van Diepen, R. S. Craig, and W. E. Wallage, Crystal field and magnetic heat capacity in PrIn and CeIn, *Journal of Physics and Chemistry of Solids* **32** (1971) 1867, https://doi.org/10.1016/0022-3697(71)90292-9

52. P. D. Dernier and J. P. Remeika, Synthesis and symmetry transformation in the perovskite compounds PbHfO and Cd- HfO, *Materials Research Bulletin* **10** (1975) 187, https://doi.org/10.1016/0025-5408(75)90111-1

53. S. A. Khan and A. H. Reshak, First principle study of electronic structure, chemical bonding, and optical properties of 5-azido- 1H-tetrazole, *International Journal of Electrochemical Science* **8** (2013) 9459, https://doi.org/10.20964/2013.07.09

54. V. B. Bobrov *et al.*, Kramers-Kronig relations for the dielectric function and the static conductivity of Coulomb systems, *Europhysics Letters* **90** (2010) 10003, https://doi.org/10.1209/0295-5075/90/10003

55. A. A. Lavrentyev *et al.*, Electronic structure and optical properties of RbPbBr, *Journal of Physics and Chemistry of Solids* **91** (2016) 25, https://doi.org/10.1016/j.jpcs.2015.11.008

56. S. Saha, T. P. Sinha, and A. Mookerjee, Electronic structure, chemical bonding, and optical properties of paraelectric BaTiO, *Physical Review B* **62** (2000) 8828, https://doi.org/10.1103/PhysRevB.62.8828

57. B. Amiri, A. Lazreg, and F. A. Bensaber, Optical and thermoelectric properties of Gd doped wurtzite GaN, *Optik* **240** (2021) 166798, https://doi.org/10.1016/j.ijleo.2021.166798